

Matthew Malkan,¹

UCLA Astronomy Division, Los Angeles, CA 90095-1562, USA

Abstract

The two major functions in galaxy evolution that we would like to measure are the stellar populations in galaxies, and their time-derivative, the star formation rate. Especially at redshifts above 1, both of these measures are benefiting greatly from wide-area infrared observations. Several space-based and ground-based examples will be discussed.

1 Understanding Galaxy Evolution with Deep Fields

Since this is a conference talk rather than a journal paper, I'll start on a philosophical note. Let's reflect on some of the good fortune observational cosmologists enjoy. The task of understanding the contents of the universe, (let alone their evolution), is so audacious, that it is remarkable we can even start doing the job. One reason we can is that gravity helpfully imposes some clear organization on how matter is arranged. Luminous mass appears (at most wavelengths) to be strikingly organized into stars and galaxies. Biologists rely heavily on their crucial organizing concepts of cell, organism and species. As astronomers, we see the world clearly arranged into self-gravitating planets, stars and galaxies. Although these categories span enormous ranges, for example in luminosity, they obey regularities and patterns. This is why we can make clear distinctions between what is or is not a star, and what is or is not a galaxy. We can, for example, distinguish individuals in these classes from bound clusters of them. These are two of the surprisingly easy categories which define our field. When we cannot use them, our job gets harder. Operationally, the star and galaxy concepts are closely linked, since we rarely think about one being present without the other. It is in fact very difficult to learn much about "galaxies" before they began forming many stars. I'll discuss one possible exception to that generalization at the end.

The last half of the 20th century saw dramatic progress in understanding the evolution and even the formation of stars. The first half of the 21st will herald similar advances in understanding the evolution and formation of galaxies. These systems are sufficiently more complicated and distant than stars that empirical, observation-driven data must play a relatively larger role than theory. (Stellar structure and evolution are rarely influenced by external circumstances. Isolated stars, for example, hardly ever experience close encounters. Galaxies often do, and their motions are often dominated by dark matter we know little about.)

Since galaxies have a wide range of (evolving) properties, we need to study large samples of them. Fortunately, they are so numerous that deep field surveys with large array detectors can provide such samples, often spanning a wide range of redshift simultaneously. Two of the most fundamental observables to derive from galaxy surveys are 1) their luminosity function (a measure of their population of formed stars) and 2) their rates of recent and ongoing star formation. In deep fields we can study how both of these evolve through cosmic time.

Of the results obtained from the Hubble Deep Field (HDF), the most far-reaching is that the star formation rate is high at $z \sim 3$ ([20],[21]), with a possible decline at $z \sim 4$. When combined with low-redshift data (e.g. [18]), there is evidence for a peak in the comoving SFR at $z \approx 1 - 2$, around a third of the Hubble Time. The apparent resemblance between this star formation rate curve and the evolution of quasars has been noted.

For both of the main goals in the study of galaxy evolution—measuring the stellar population, and its first time derivative—observations with large-format (*e.g.* million-pixel) infrared detectors are essential. I will illustrate this by reviewing several applications of infrared observations. Some of these were also discussed at a Tokyo conference of the Birth and Evolution of the Universe ([24]). Even though only two years have passed, so many advances have been made, that an update is due.

¹E-mail:malkan@astro.ucla.edu

2 Detecting Evolving Stellar Populations Across Cosmic Time

Deep multicolor imaging is our most powerful tool for understanding galaxy evolution. Broadband filter measurements can go very deep; the resulting spectral energy distributions provide estimates of the photometric redshifts of distant galaxies. The Hubble Space Telescope, with its superb spatial resolution, provides deep detections, along with detailed measurements of galaxy morphologies, in small fields. Large CCD cameras on ground-based telescopes provide complementary coverage of much larger areas (e.g. in [31], and the Sloan Digital Sky Survey.) The next step, intensive spectroscopic follow-up (e.g., [39]) has been rewarded with the detection of many hundreds of galaxies at redshifts of around 1 and 3. Most galaxies at $z \geq 3$ have been discovered using the powerful Lyman break/U-band drop out selection method (e.g., [40]). This method, which is currently confined to $z \sim 3 - 4$, does not of itself provide an accurate confirmed redshift. Follow-up optical spectroscopy is still needed. The Lyman break method falters at $z < 2.7$ because at that redshift the Lyman limit has not yet cut out much of the continuum in the U-filter. Lyman break galaxy (LBG) surveys are not possible in the redshift 2 range.

The intermediate redshift range around $z \sim 2$ appears to be the epoch during which the familiar components of modern galaxies assembled. A significant percentage of the universe's evolution (≈ 3 Gyr), or 25% of its total age, occurred from $z=1$ to 3, as opposed to the more distant and better-studied $z=3-4$ range, which covers ≈ 0.5 Gyr, or only 5% of cosmic time. This intermediate epoch can be dubbed the "Bright Ages", since it appears to be the time when most stars in the Universe formed (and most heavy elements were produced).

However, our observational knowledge of galaxies in the crucial range of $z = 1.5 - 2.5$ is surprisingly sketchy. Due to severe limitations of optical search and confirmation methods, we are in the odd position of knowing more about the most distant galaxies than those closer. Continuum observations at $\lambda \geq 4000\text{\AA}$ are needed to assess the build-up of evolved stars. Similarly, the most useful emission lines for measuring gas photoionized by recently formed stars are in the rest-frame optical. Thus the most reliable measures of total stellar mass as well as current star formation rates (the first derivative of the former) are obtained in the near-infrared for redshifts in the Bright Ages.

2.1 Near-Infrared Searches for Galaxies in the Bright Ages

Some of the early successes in identifying non-active, non-lensed galaxies at high redshifts came from searches for strong emission lines with narrow-band filters. This method provides accurate redshifts, but selects from a limited range of redshifts and has yielded only a modest number of detections (e.g., [27], [28], [9]).

Optical multicolor photometry alone works well at measuring the Balmer break up to $z \sim 1$. Infrared photometry makes it possible for us to identify Balmer break galaxies at $1.5 \leq z \leq 2.5$. New large-format detectors are able to make sensitive surveys in the near-IR wavebands, especially with the key $2.2 \mu\text{m}$ (K) band. This allows us to measure the second strongest spectral feature in galaxies—the Balmer break, from around 4000\AA to 3650\AA . This blue-side drop is nearly always strong in populations of young or old stars (although its wavelength shifts slightly redward in older galaxies).

Figure 1 shows the V, I, J and K bandpasses superposed on the model spectrum of a galaxy at $z=1.5$. To reach $z=2.5$ requires good photometry in the K filter, so that at least one point in the spectral energy distribution is cleanly on the *red* side of the Balmer break. Two-color plots are useful for identifying galaxies likely to lie in the Bright Ages epoch. An example is shown in Figure 2. Models with a variety of star-formation histories are shown for galaxies with $0 \leq z \leq 1$ by the crosses; models with $1 \leq z \leq 2$ by the diamonds, and $2 \leq z \leq 3$ with the small dots. In the astro-ph version I color-coded these model predictions based on their V-I colors. The open squares show galaxy photometry from one of our deep fields imaged on the Lick 3-m telescope.

The $3600/4000\text{\AA}$ break is less strong than the Lyman break. Nonetheless, by fitting the full galaxy multiwavelength spectral energy distribution to redshifted galaxy templates we can estimate its photometric redshift to an accuracy of one or two tenths in z (e.g., [17], [8], [3], [13]). Infrared flux points greatly improve the accuracy of the method [7]. To demonstrate the power of this method, we present a six band (B through K) picture of an very red object [6]. Figure 4 shows the photometric redshift fit to its BVIJHK spectral energy distribution, using Hyperz ([2]). The infrared bands were crucial not only in identifying this as an interesting object, but allowing a fit to data beyond the 4000\AA break. The

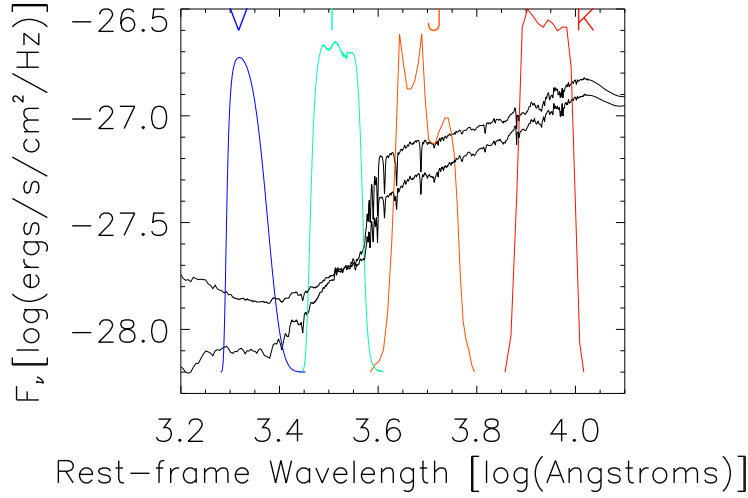


Figure 1: The VIJK filter set superposed on typical galaxy spectra at $z=1.5$. The representative Spectral Energy Distribution for the galaxy is from the GISSEL spectral synthesis models. The Balmer break produces a very red I-J color. As the redshift increases above 1.5, the shift in the Balmer break makes J-K redder than 2.

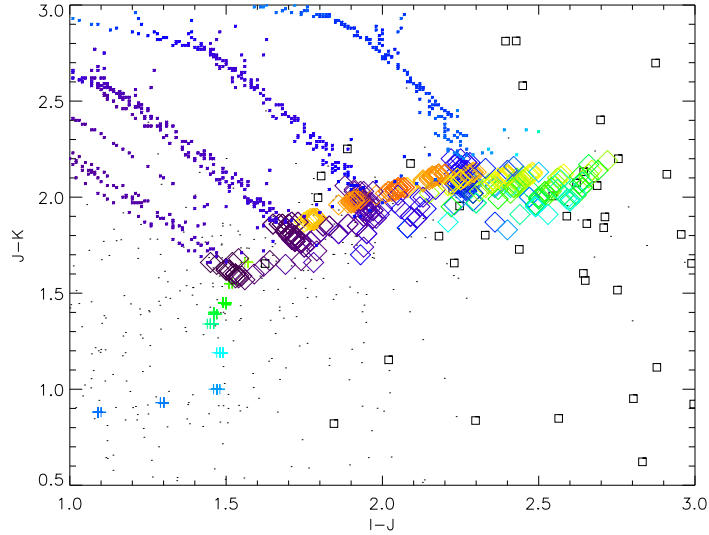


Figure 2: The the I-J, J-K plane for model galaxies at redshifts from 0 to 5. In the astro-ph version, additional V-I information is encoded in color (with the bluest values shown as the bluest points). The colored points outline tracks for Bruzual and Charlot stellar evolution models of galaxies with initial formation epochs at high redshift which then have superposed more recent starbursts of varying strengths. The limited grid of starburst epochs ($z=2.6, 2.8, 3.0, 3.5, 5$) produces the several different locations of the “peeling back’ in the two-color diagram. Note that the rest-frame UV light (shifted into the B+V bands) is extremely sensitive to the temporary presence of young stars, while the rest-frame optical (in the J and K bands) is insensitive to them. The open squares show our measurements of galaxies in one of the deep fields we observed with the Gemini 2-channel infrared camera on the Lick 3-m telescope.

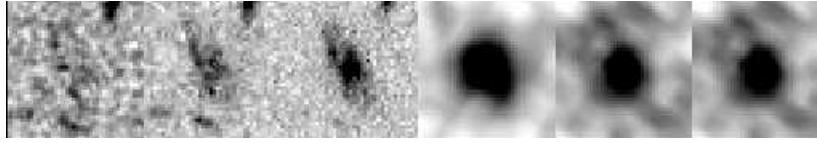


Figure 3: Mosaic of reduced multicolor images of a $4 \times 4''$ box around a galaxy in the 53W002 field with photometric redshift $z = 1.12$. Wavelength increases from B at the left to K on the right; the object can qualify as an “Extremely Red Object” (ERO), with $V - K > 6$. The smooth round bulge becomes progressively more dominant at longer wavelengths, while at the shorter wavelengths the galaxy appears patchy with irregular arms.

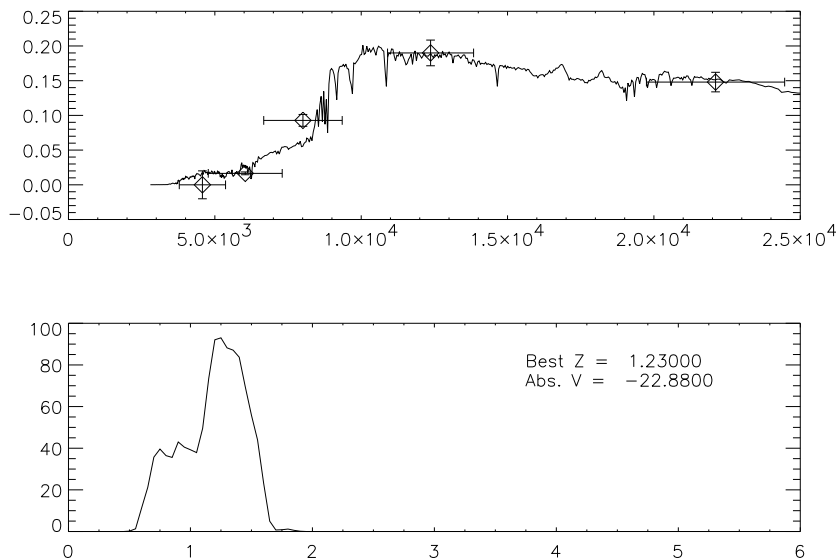


Figure 4: BVIJK photometry we measured for an “extremely red” galaxy in the MTM0953+549 field. Note the sudden jump at the Balmer break, which makes a very large V-J color, even though the J-K is not unusually red. The best-fitting spectral template, at $z=1.23$ is overplotted in the top panel. The lower panel shows the probability distribution of acceptable redshifts fitted by the photometric redshift engine. The best fit implies the galaxy has $M_V = -22.9$.

fit estimates its redshift, $z=1.23 \pm 0.25$, and also that it is a 0.5 Gyr old burst of star formation with $A_V = 1.2$ mag of dust extinction. The infrared photometry provides a fairly good estimate of the total stellar mass.

A lot of what we think we know about high-redshift galaxies rests on the limited statistics of photometric redshifts in the Hubble Deep Fields, mostly HDF-N. The HDF-N has 150 galaxies with photometric redshifts in the Bright Ages ($1.8 \leq z \leq 2.6$). However, only 8 of these are spectroscopically confirmed after extensive efforts, and *no* Bright Ages galaxy candidates in HDF-S have confirming spectra yet. Major conclusions have been drawn from analysis of one $2.6' \times 2.6'$ image of the Universe. This is particularly dangerous since LBG surveys have found large field-to-field variations—up to a factor of four in surface density—due to large-scale structures, which also appear as spikes in redshift histograms. Since our view of galaxies depends strongly on which sight-line we observe, *it is imperative to investigate galaxy evolution in several regions with similarly deep data*. Many efforts, both ground- and space-based, are currently underway to do this, for example at Subaru ([22]), VLT (VIRMOS/DEEP) and NOAO (Deep Wide-Field Survey).

Figure 5: Our WFPC-2 continuum-subtracted $H\alpha$ image of “Early-Type” Galaxy NGC 2328 from Glassman and Malkan [10], shown as a greyscale plot. The optical continuum is shown with overplotted contours. The field of view is roughly $6 \times 10''$.

3 Evolution of Star Formation is also well traced in the infrared

A region’s “current” star formation rate (SFR) is approximately proportional to its population of upper main sequence stars, because of their cosmically brief lifetimes. The presence of massive stars is manifested in several observables which are not strongly produced by old stellar populations: a) direct photospheric radiation, predominantly in the UV. At lower frequencies it extends into the optical, where it produces blue colors in a stellar population. The high-frequency tail extends above 1 Ryd, and includes a substantial fraction of ionizing photons, in the hottest stars. Much of this radiation is absorbed by gas and re-emitted as b) nebular emission lines, mostly in the optical and infrared. The most massive stars hardly live long enough to completely leave the dusty environments in which they were born. Thus, much of their remaining continuum emission may be absorbed by interstellar dust grains, which are warmed to c) re-emit the power thermally in the infrared. Finally, massive stars are the most violent sources of mechanical energy in the ISM, driving winds and supernovae. A fraction of this power accelerates electrons which then emit d) synchrotron radiation.

After a great deal of work on the alternatives, it is $H\alpha$ line emission which remains the “gold standard” of SFR measurements. It is equivalent to counting the ionizing continuum photons from the hottest (youngest) main-sequence stars at a wavelength that is relatively insensitive to absorption. The observable line luminosity is supposed to equal a constant times the aggregate SFR: $L(H\alpha) = 1.1 \times 10^{41}$ erg/sec per $M_{\odot}/year$ [16].

By contrast, the other leading SFR indicator at high redshift—the ultraviolet continuum—is far more sensitive to dust reddening. The integrated star-forming luminosity of those LBGs *detected* needs to be corrected upward for extinction by a factor of 2 – 7 ([32], [33], [1], [14], and [38]). Furthermore, these LBGs were selected to be the *least* dusty ones.

We can obtain a better idea of why the line and continuum SFR estimates disagree (methods a and b above) by looking closely (with HST) at nearby star-forming galaxies. The contours in Figure 5 show our HST imaging of the (continuum-subtracted) $H\alpha$ emission in the small star-forming galaxy NGC 2328. The greyscale shows the optical continuum, which has a considerably different spatial distribution. Note the numerous contour peaks with little or no associated optical light. These HII region complexes with significant reddening account for the majority of the current star formation in this galaxy. Another even more dramatic example of a dust-enshrouded starburst is seen in the nearby galaxy NGC 5253 [11].

Although $H\alpha$ gives a more complete census of recent star formation, it cannot be measured with CCD spectrographs for $z \geq 0.5$. Even the weaker and less reliable $H\beta$ line is shifted out of the optical range at $z \geq 1$. Fortunately, they are still measurable in the near-infrared. Two methods—one ground-based and one space-based—have been successful.

3.1 Narrow-Band Infrared Imaging of Emission-Line Galaxies

Large-format multislit spectrographs are not yet available in the near-IR. This will change when instruments such as the NIRMOS (Near-infrared Multi-Object Spectrograph) begin working on the VLT, and

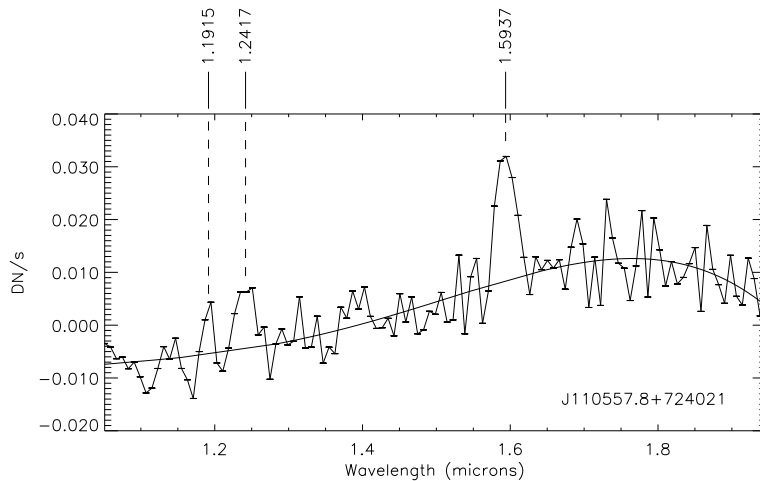


Figure 6: Extracted spectrum of a star-forming galaxy discovered in a deep NICMOS-grism parallel observation (Malkan et al. [23]). At a redshift of 1.49, this low-resolution spectrum shows both $H\alpha$ and $H\beta$, as well as a broad blend of the two [OIII] doublet lines, the redshifted 5007 and 4959Å emission.

Flamingos (in multi-slit mode) on Gemini. For now, ground-based searches are restricted to either narrow spatial or spectral windows. The latter case is obtained with narrow-band interference filter imaging. To speed up the detections, there is often a pre-selection of special fields. These are supposed to have excess galaxies at the targeted redshift, because some object in the field is already known to have that z . Several dozen galaxies at redshifts above 2 have been discovered by detecting their $H\alpha$ line emission ([27], [28], [4],[15], [29]). More discoveries will be coming soon with the availability of 1K x 1K near-infrared array detectors.

3.2 Grism Spectroscopy

Slitless spectroscopy receives the full sky background from the entire spectral window at each point on the detector. It is therefore impractical with ground-based infrared telescopes. However, it has been demonstrated to work very well in space, where the backgrounds are much lower. In particular, the NICMOS Camera 3 on HST has an objective grism that disperses the spectra of all objects within its 50'' field-of-view. Since it was able to operate simultaneously with other HST instruments, it obtained a substantial number of deep parallel pointings on random fields. The largest set of these were reduced and analyzed by McCarthy et al. [30]. The exposures of a few orbits had a 1 in 3 chance of detecting a line-emitting object in the field; in the longer parallel observations, these odds increase to nearly 100%. In addition, a single very deep NICMOS grism field was observed during a 3-day pointing in the Continuous Viewing Zone ([23]).

The standard assumption in deep near-IR grism surveys of random fields is that any single emission line detected is redshifted $H\alpha$. In only one of the dozen cases tested so far has this assumption been shown to be incorrect; it is likely true better than 90% of the time. This allowed Yan et al. [42] to estimate the global luminosity function of recent star formation in the $0.8 \leq z \leq 1.7$ universe.

In some cases, the difficult confirmation with optical spectroscopy is not even necessary because a second emission line is also detectable simultaneously in the NICMOS grism image. Figures 6 and 7 show deep grism spectra (observed wavelengths) in which emission lines other than $H\alpha$ are detected. In Figure 6 the additional lines on the blue side are $H\beta$, and the [OIII]5007/4959 doublet, at $z_e = 1.49$. In Figure 7 the only emission-line spectrum which does *not* show $H\alpha$ is shown. This foreground ($z_e = 0.35$) galaxy shows the strong emission lines of He I 1.083/ $P\gamma$ 1.093 μm , [FeII]1.257 and $P\beta$ 1.281 μm [23].

In its first incarnation, this camera was defocused by the distortion of the NICMOS dewar. This degraded the spatial resolution to about 0.4''. The resulting spectral resolution was only $R \sim 50$. Hopkins et al. [14] used NICMOS Camera 3 for pointed observations of suspected high-redshift galaxies during a campaign when it was in focus. Both their observations and the parallel ones indicated that SFR rates estimated from $H\alpha$ emission in galaxies at $0.8 \leq z \leq 1.7$ are several times higher than those estimated from their UV continuum.

These large numbers of strong $H\alpha$ -emitting galaxies already indicate that search methods using shorter wavelengths are incomplete. Similar incompleteness in surveys of star formation rates has also been found in the local universe by Sakai et al. [35]. If short-wavelength surveys really do miss a substantial

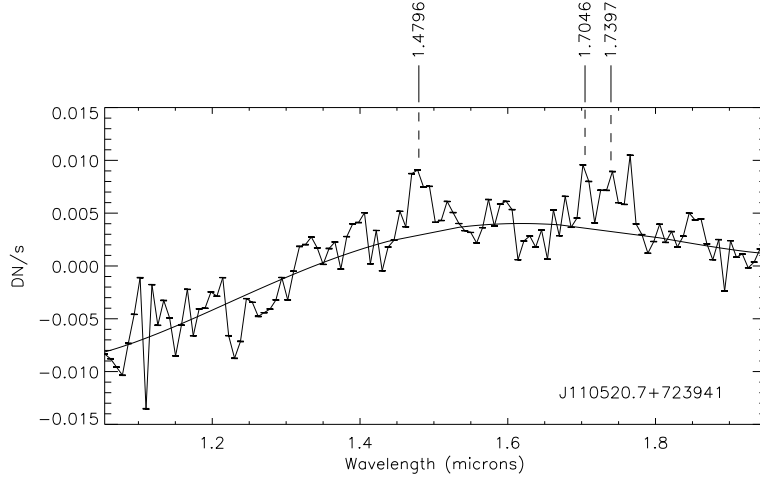


Figure 7: Another star-forming galaxy in the same NICMOS parallel field [23]. This is the only grism spectrum in which none of the detected emission lines is $H\alpha$. The lower redshift, $z_e = 0.35$, allows the detection of the He I 1.083/ $P\gamma$ 1.093 μm blend and the [FeII]1.257 and $P\beta$ 1.281 μm emission lines.

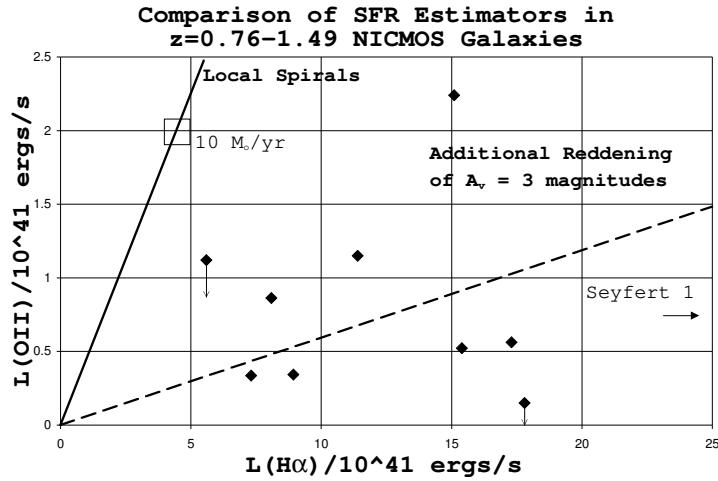


Figure 8: Comparison of star formation rates estimated from [OII]3727 and $H\alpha$ line emission, in $z \geq 1$ galaxies discovered by the NICMOS grism. Typical uncertainties on the points are 20–30%. The open square indicates the line luminosities predicted by the local relations for an SFR of $10M_{\odot}/\text{year}$. All of these 9 galaxies observed at Keck by Hicks et al. [12] have relatively weaker [OII] emission than would be predicted by their $H\alpha$ line, based on local spiral galaxies (which are described by the solid line). Instead, their [OII]/ $H\alpha$ ratios are suggestive of additional internal dust absorption, which might be as large as $A_V = 3$ mag (shown by the dashed line).

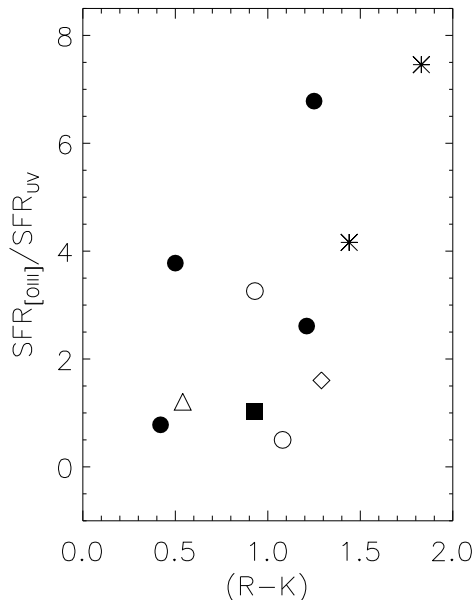


Figure 9: The ratio of star formation rates estimated by [OIII]5007 and UV continuum emission from 10 Lyman break galaxies [38]. [OIII] for the open circles and asterisks was measured from narrow-band imaging; for the remaining points it comes from slit spectroscopy. The [OIII] line reveals several (up to seven) times more current star formation than does the UV continuum, especially in the redder galaxies. This is probably largely attributable to internal dust reddening.

amount of obscured star formation activity, we should examine galaxies that are found in the near-IR, to see if they are indeed dustier than those discovered by optical surveys. In Figure 8 we compare the two emission-line indicators of current star formation rates— $H\alpha$ and [OII]3727 luminosities. The nine data points represent the NICMOS-selected galaxies, with followup Keck optical spectra from Hicks et al. [12]. The solid line shows the observed average ratio in local spirals, which does not fit the NICMOS galaxies. In these IR-selected galaxies the [OII] line systematically underestimates the SFR. This discrepancy between the two indicators cannot be predicted from the broadband colors, which are not often extremely red. Many of these galaxies must contain additional internal reddening around their star-forming regions. The dashed line shows an indicative amount, of $A_V = 3$ mag. If the ten galaxies we measured are representative of $H\alpha$ selection in general, it produces samples of galaxies which a) would mostly be missed by optical search methods; and b) still need a significant upward correction for dust extinction. We need $H\alpha$ and short-wavelength SFR measurements for more of the *same* galaxies to see how much overlap there is between those selected with optical and IR searches.

3.3 Nebular Diagnostic Line Emission at Higher Redshift

$H\alpha$ is redshifted beyond the prime sensitivity of infrared detectors at $z \geq 2.6$. By unlucky coincidence, the rising thermal background makes it impossible to compare star formation rates from $H\alpha$ with those estimated from the ultraviolet continuum in the LBGs. Thus the only way to make a *direct* comparison of SFR indicators (*i.e.*, on the same galaxies) is by replacing $H\alpha$ with another emission line that is bluer in the optical rest-frame, and less reliable. The advantage of using $H\beta$ as this “silver standard” SFR estimator is that its intrinsic strength relative to $H\alpha$ is known accurately from recombination theory [33]. The [OIII] 5007 and 4959Å doublet, however, is usually two or three times stronger, and is not so affected by underlying stellar absorption. In Figure 9 we compare the star formation rates predicted by [OIII] and UV continuum emission in eleven LBG’s at $z \sim 3$. A few galaxies lie near the bottom of the graph, consistent with 1-to-1 agreement. However in most of them, the [OIII] line emission predicts a higher SFR by a factor of 3 to 7 times. This is again consistent with the amounts of internal dust reddening that have been inferred from other observations.

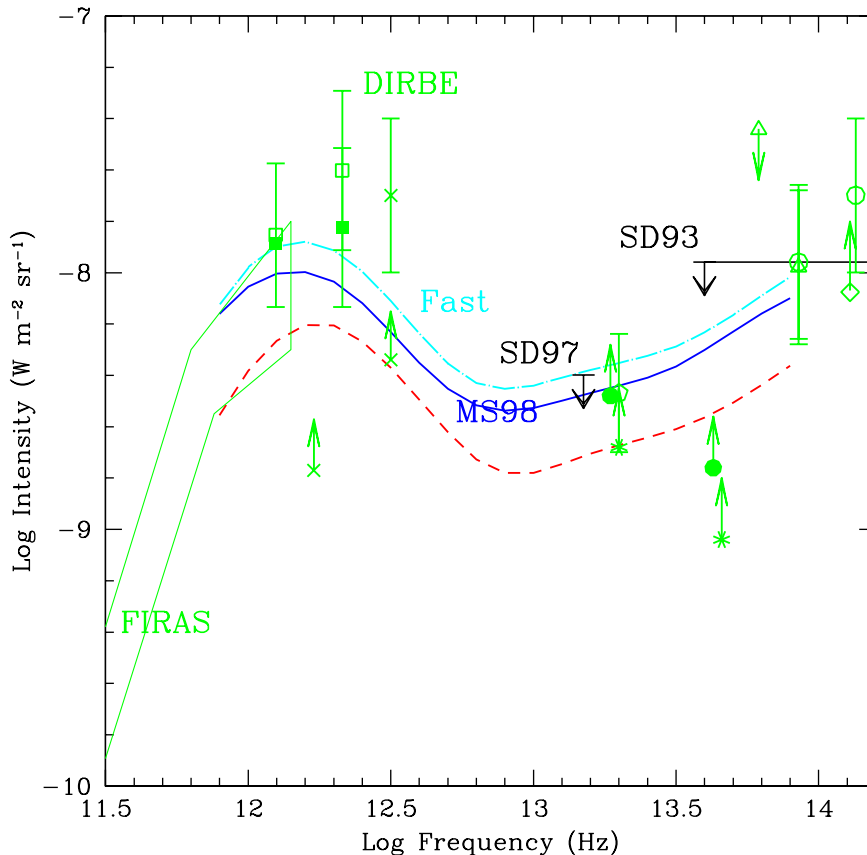


Figure 10: Model predictions of the Diffuse Infrared Background Emission from galaxies, compared with observations, from Malkan and Stecker [26]. The “best guess” baseline evolutionary model shown by the middle line, assumes that infrared luminosities of galaxies increase as $(1+z)^3$ from $z=0$ back to $z=2$. The most rapid evolution model, shown by the upper (“Fast”) line, assumes luminosity evolution as $(1+z)^4$ back to $z=1.4$, and is also marginally consistent with all the observations. The lower limits are set by deep number counts obtained with the Infrared Space Observatory. The two lines with upper limits are set by the absence of high-energy absorption in the gamma-ray spectra of distant blazars, from Stecker and DeJong. Most of these strong observational constraints became available *after* the MS models were first published.

4 The Promise of Space Imaging Surveys in the Thermal Infrared

The thermal dust emission, (method “c” above) can estimate the high-redshift SFR with hardly any sensitivity to extinction. Instead of measuring the primary signatures of hot young stars— their UV continuum and resulting ionized gas—we can measure this emission after it is reprocessed by dust, since that is where much (probably most) of the energy ends up before escaping the galaxy. This secondary thermal continuum is emitted mostly at $25\text{--}60\ \mu\text{m}$. Since this continuum emission can dominate the entire bolometric luminosity of a dusty star-forming galaxy, it is now detectable out to high redshifts.

First, it can be detected globally, by wide-area measurements of the Diffuse Infrared Background (DIRB) radiation. New observations continue to define the DIRB more and more accurately, over a wide wavelength range (from $2\text{--}500\ \mu\text{m}$). It is surprisingly bright, and requires strong cosmic evolution in the population of dusty galaxies at $z \sim 1$ (*e.g.*, [25]). “Backwards evolution” models, which are based on our empirical knowledge of infrared emission from local galaxies, have also improved. Figure 10 illustrates a recent comparison between these models and DIRB observations, from Malkan and Stecker [26]. Two plausible evolutionary scenarios are shown – a baseline model with pure luminosity evolution going as $(1+z)^3$, and a “Fast” evolution scenario that reaches the same maximum luminosities at an earlier z , 1.4 rather than 2.0. As shown in Figure 11, this latter scenario is somewhat more consistent with independent estimates of the cosmic SFR evolution, compiled by Rowan-Robinson [34].

Upcoming deep IR surveys from space will soon resolve this background. The key is surveying enough area with sufficient sensitivity to detect “typical” galaxies at the desired redshifts. “Typical” can be defined by the characteristic knee in the galaxy luminosity function, which is well defined at $z=0$, and appears to be more luminous at high redshifts [40]. Although such “ L_* ” galaxies are not very numerous

Figure 11: Comparison of the luminosity evolution model from Malkan and Stecker (1998 and 2001, [25], [26]) with estimates of the global evolution of star formation rates. The baseline evolution, and rapid evolution models of MS are shown by the light and dark solid lines, respectively. Both assume no evolution from z of 2 up to 5. Error bars are estimates from Rowan-Robinson [34] based on a variety of observational methods, with substantial corrections for dust extinction applied.

in a standard Schechter luminosity function, galaxies of L_* or brighter do produce more than 16% of the total integrated galactic luminosity. And in flux-limited samples, where the number of galaxies detected gets weighted like $L^{3/2}$, half of the total luminosity will come from galaxies of $0.7 L_*$ and brighter. Figure 12 shows the Malkan and Stecker predictions for the observed fluxes of L_* galaxies back to redshift 5, for 3 different wavelengths. Note that they do not fade much from $z=0.5$ to 2 because of their strong luminosity evolution.

SIRTF, in its “First Look Survey”, and Astro-E (IRIS), in a wider sky survey, will have the sensitivity needed to detect the typical L_* galaxies at $z \geq 1$ which are expected to dominate the DIRB. As shown in Figure 13, the longest cosmological reach is provided by observations at $6 \mu\text{m}$ (with SIRTF) and $200 \mu\text{m}$ (with FIRST), since these wavelengths are redward of the two peaks in the spectra of galaxies. This results in “negative K-corrections”, the reverse of the usual situation in which higher redshifts shift a relatively fainter part of the galactic spectrum into our fixed observing bandpass.

5 Damped Ly α Absorption from Pregalactic Objects?

Implicit in the previous discussion is the assumption that the “birth of a galaxy” is operationally equivalent to the epoch of its first major burst of star formation. This is usually the first chance we have to detect objects which will eventually evolve into modern galaxies. However, damped Ly α absorption systems (DLAs), detected as neutral hydrogen troughs ($N_{HI} \sim 10^{20-23} \text{cm}^{-2}$) in the spectra of high- z quasars, detect baryonic concentrations independent of star formation or nonstellar nuclear activity. DLAs contain most of the H I in the universe.

Imaging searches for galaxies associated with DLAs are not new, but they have been almost impossible to carry out from the ground [19]. They are best performed in the near-IR, where the DLA starlight should be relatively bright compared to the background quasar. Unfortunately, a large enough H I column density to be detected as a DLA is only expected to occur at small impact parameters through a galaxy (or protogalaxy) – within 10 or 20 kpc of its center ([41]). This corresponds to a separation between the galaxy and the line-of-sight to the background quasar of less than 1 to $2''$. Detecting a faint galaxy this close to a bright source is exceedingly difficult from the ground. Adaptive optics is not yet the solution (beset by poor Strehl ratios). Proposed interferometric techniques are more suitable for detecting a compact source at a known position angle with respect to the quasar (and still the required

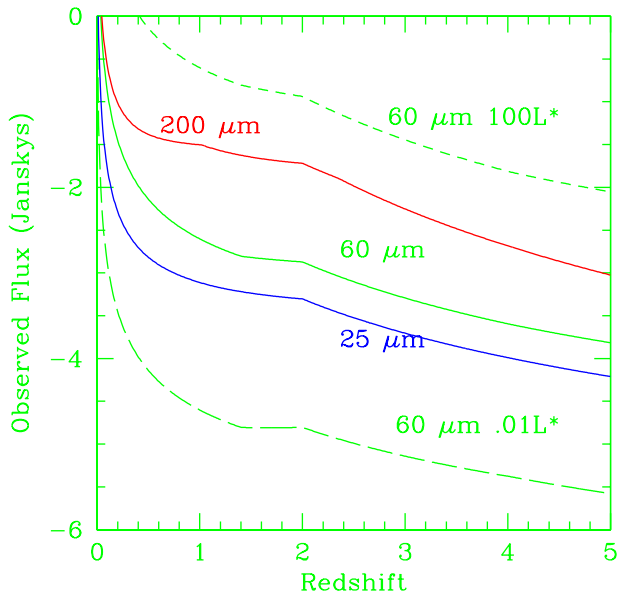


Figure 12: Predicted brightness at infrared wavelengths of an L_* galaxy, from Malkan and Stecker [26], at 25, 60 and 200 μm . The dotted lines show the predicted brightnesses for galaxies 100 times above and below the characteristic L_* knee of the luminosity function. There is a kink at $z=2$, beyond which the galaxy luminosity evolution is assumed to level off.

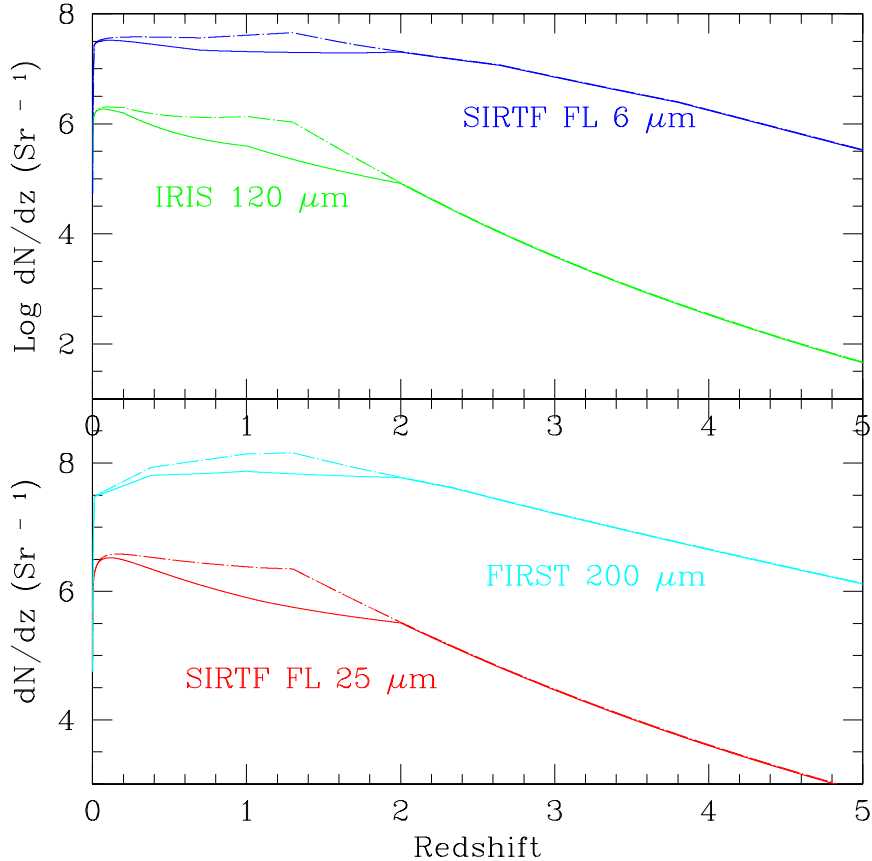


Figure 13: Predicted logarithmic number counts per unit redshift for galaxy luminosity evolution models in Malkan and Stecker [26]. The higher line, shown by dashes, illustrates the “Fast evolution” model.

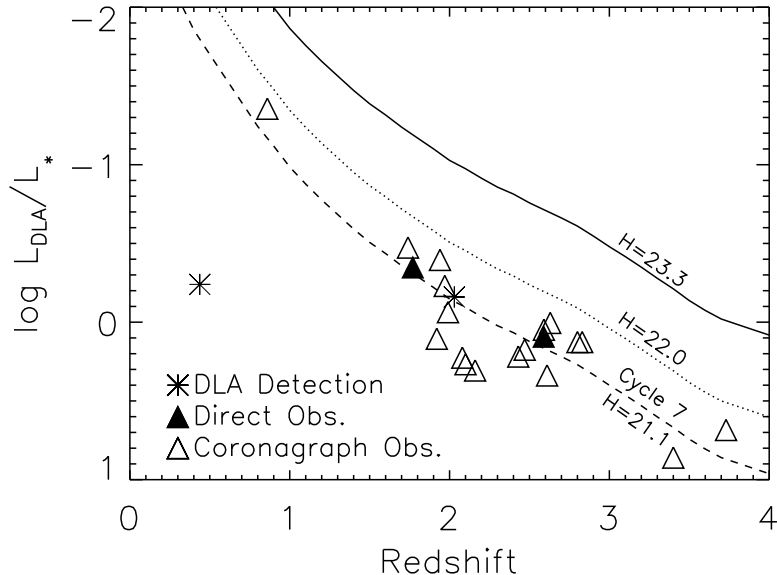


Figure 14: Upper limits to the $1.6 \mu\text{m}$ continuum emission from starlight associated with Damped $\text{Ly}\alpha$ Absorbers, from Colbert and Malkan ([5]). Since they are all limits (except for the two plausible detections shown by asterisks), they are pointing upwards (towards less luminous galaxies). These upper limits would be a factor of two tighter for any galaxies more than $1''$ away from the quasar (ie., they understate the true sensitivity of the observations). The dashed, dotted and solid lines illustrate typical $5 - \sigma$ upper limits obtained in our Cycle 7 program, and future possible NICMOS observations with somewhat longer, and much longer integration times. For twenty observed DLA systems, our HST coronagraphic imaging rules out the possibility of a galaxy having typically a luminosity of $0.7\text{--}1.0 L_*$.

dynamic range may be unattainable). Ground-based imaging can discover DLA galaxies *only* at large impact parameters, greater than 25 kpc (for $H_0 = 75$). To do better, an extremely sharp and stable PSF is required, preferably near the diffraction limit. This means going into space.

We therefore used the NICMOS-2 camera on the HST in coronagraphic imaging mode to search for near-IR continuum emission from starlight associated with two dozen DLAs. Our results are shown in Figure 14. Despite the approval of 95 targets, only two dozen quasar observations were attempted, and many were not as sensitive as they could have been. This low success rate was because: 1) the coronagraph was not fully operational during the first half of Cycle 7, 2) SNAPSHOT proposals utilizing the coronagraph were not scheduled for a few months after the coronagraph became operational, and 3) failure of the coronagraph to autonomously acquire several of the quasars when they were scheduled resulted in a loss of those observations. Despite these difficulties, we detected two likely DLA galaxies of $\sim 0.7L_*$, and obtained upper limits for nearly twenty DLAs ([5]). Our 5σ upper limits for the continuum fluxes of the DLAs are plotted in terms of L_* versus redshift in Figure 14. Note that the vertical axis has logarithmic luminosity increasing downwards—higher observations are more sensitive to fainter galaxies. The only detections of possible DLA galaxies are shown by the two asterisks. The lowest curve is our measured sensitivity for Cycle 7; filled triangles represent direct imaging, while open triangles represent coronagraphic observations. The middle curve shows our predicted sensitivity in a 1300-second NICMOS integration, a half magnitude gain over our current limits. Finally, the upper curve is the predicted sensitivity of for “limiting” 10,000-second exposures, would push detection limits 2 mags fainter.

There were only two plausible DLA detections and the best upper limits were $H \sim 21.5$ mag. When we account for the fact that more luminous galaxies are likely to have larger HI cross sections, we would have expected to detect 5 or 6 of the galaxies. If the DLAs were drawn from the general galaxy population, we should have detected 2 or 3 with $1.0L_*$ or brighter, instead of zero. This discrepancy indicates that the luminosity function of DLAs is not consistent with the normal galaxy population. The objects associated with DLAs are on average fainter than normal galaxies we measure at either $z=0$ or 3. Deeper NICMOS/HST imaging can test the possibility that they are produced by dwarf galaxies such as the Magellanic Clouds.

If deeper proposed NICMOS imaging of DLA systems continues to set even stricter upper limits on their continuum emission, it may be that DLAs trace a substantial baryon reservoir not associated with normal galaxies.

I thank James Colbert, Harry Teplitz and Erin Hicks for some of the figures from our ongoing research collaborations.

References

- [1] K. Adelberger and C. Steidel 2000, *ApJ* 544, 218.
- [2] Bolzonella et al. 2000, *A&A*, 363, 476.
- [3] R. Brunner et al. 1997 *ApJLett* 482, L21.
- [4] A. Bunker, in *The Hy-Redshift Universe: Galaxy Formation and Evolution at High Redshift*, Proc. of conf. in Berkeley, CA, 21-24 June, 1999. ASP Conference Proceedings, Vol. 193, Eds. by Andrew J. Bunker and Wil J. M. van Breugel (1999), p.448.
- [5] J. Colbert and M. Malkan, *ApJ*, in press.
- [6] J. Colbert, M. Malkan, and R. M. Rich *ApJ*, in prep.
- [7] A. Connolly et al. 1997 *ApJLett*, 486, L11.
- [8] Fernandez-Soto et al. 1999, *ApJ*, 513, 34.
- [9] Francis, P. J. et al. 1996 *ApJ* 450, 497
- [10] T. Glassman and M. Malkan 2002, *ApJ*, in press.
- [11] Gorjian, Varoujan, Turner, Jean L., and Beck, Sara C. 2001, *ApJLett* 544, L29.
- [12] E. Hicks, et al. 2002, *ApJ*, submitted.
- [13] D. Hogg, et al. 1998, *ApJ*, 504, 622.
- [14] Hopkins, et al. 2000 *AJ* 120, 2843.
- [15] Kawara, et al. 1998 *A&A* 336, L9.
- [16] R. Kennicutt 1983 *ApJ* 272, 54.
- [17] D. Koo 1985, *AJ*, 90, 418.
- [18] S. Lilly et al. 1996, *ApJ Lett* 460, L1.
- [19] Lowenthal, J. D., Hogan, C. J., Green, R. F., Woodgate, B., Caulet, A., Brown, L. and Bechtold, J. 1995, *ApJ* 451, 484.
- [20] P. Madau et al. 1996, *MNRAS*, 283, 1388.
- [21] P. Madau et al. 1998, *ApJ*, 498, 106.
- [22] T. Maihara et al. 2001, *PASJ*, 53, 25.
- [23] M. Malkan et al. 2002, *ApJ*, in prep.
- [24] M. Malkan 2001, *Proceedings of Fourth RESCEU International Symposium, Our Second Look at the Immature Universe: The Infrared View*, eds. K. Sato and M. Kawasaki (Univ. Acad. Press: Tokyo), 119.
- [25] M. Malkan and F. Stecker 1998, *ApJ*, 496, 13.

- [26] M. Malkan and F. Stecker 2001, ApJ, 555, 641.
- [27] M. Malkan, Teplitz, & Mclean (MTM) 1995, ApJ, 448L, 5.
- [28] M. Malkan, Teplitz, & Mclean 1996, ApJ, 468L, 9.
- [29] F. Mannucci et al. 1998 ApJLett, 501, L11.
- [30] McCarthy, P. et al. 1999, ApJ 520, 548.
- [31] M. Ouchi 2001, ApJLett, 558, L83.
- [32] Pettini, M., Kellogg, M., Steidel, C.C., Dickinson, M., Adelberger, K. L., & Giavalisco, M., 1998, ApJ 508, 539.
- [33] Pettini, M. *et al.* 2001, ApJ 554, 981.
- [34] M. Rowan-Robinson 1999 ApSpSci, 266, 291.
- [35] S. Sakai, R. C. Kennicutt, and C. Moss 2000, in Galaxy Disks and Disk Galaxies, eds. J. G. Funes and E. M. Corsini (ASP Conf. Ser.), 329.
- [36] H. Teplitz et al 1998, ApJ, 506, 519.
- [37] H. Teplitz, H.I, Malkan, M.A., & McLean, I.S., 1999, ApJ 514, 33.
- [38] H. Teplitz et al 2000, ApJ 542, 18.
- [39] C. Steidel et al. 1996, AJ, 112, 352.
- [40] C. Steidel, C.C., Adelberger, K.L., Giavalisco, M., Dickinson, M., & Pettini, M. 1999, ApJ 519, 1.
- [41] Wolfe, A. M. 1988, in QSO Absorption Lines: Probing the Universe, ed. J. C. Blades, D. A. Turnshek, and C. A. Norman (Cambridge: Cambridge University Press), 297
- [42] Yan, L. et al. 1999 ApJ Lett 519, 47.

This figure "figure5.gif" is available in "gif" format from:

<http://arxiv.org/ps/astro-ph/0110357v1>

This figure "figure11.gif" is available in "gif" format from:

<http://arxiv.org/ps/astro-ph/0110357v1>